



Chemical and in vitro characterizations of a promising bimodal AGuIX probe able to target apoptotic cells for applications in MRI and optical imaging

Mario Dentamaro, François Lux, Luce Vander Elst, Nicolas Dauguet, Sylvie Montante, Albert Moussaron, Carmen Burtea, Robert N. Muller, Olivier Tillement, Sophie Laurent

► To cite this version:

Mario Dentamaro, François Lux, Luce Vander Elst, Nicolas Dauguet, Sylvie Montante, et al.. Chemical and in vitro characterizations of a promising bimodal AGuIX probe able to target apoptotic cells for applications in MRI and optical imaging. *Contrast Media and Molecular Imaging*, 2016, 11 (5), pp.381 - 395. 10.1002/cmmi.1702 . hal-01405753

HAL Id: hal-01405753

<https://hal.science/hal-01405753>

Submitted on 12 Feb 2021

HAL is a multi-disciplinary open access archive for the deposit and dissemination of scientific research documents, whether they are published or not. The documents may come from teaching and research institutions in France or abroad, or from public or private research centers.

L'archive ouverte pluridisciplinaire **HAL**, est destinée au dépôt et à la diffusion de documents scientifiques de niveau recherche, publiés ou non, émanant des établissements d'enseignement et de recherche français ou étrangers, des laboratoires publics ou privés.

Chemical and *in vitro* characterizations of a promising bimodal AGuIX probe able to target apoptotic cells for applications in MRI and optical imaging

Mario Dentamaro^{a,b,c,*}, François Lux^b, Luce Vander Elst^{a,c},
Nicolas Dauguet^d, Sylvie Montante^a, Albert Moussaron^e, Carmen Burtea^a,
Robert N. Muller^{a,c}, Olivier Tillement^b and Sophie Laurent^{a,c,*}



Different studies on AGuIX nanoparticles have been achieved in the biomedical domain, showing that they allow us to combine multimodal and theranostic properties in oncology. The targeting of apoptotic cells presents a wide range of biomedical applications, including the monitoring of antitumoral therapy and the diagnosis of diseases related to this process, such as atherosclerosis, ischemia, chronic inflammation or autoimmune disorders. AGuIX nanoparticles functionalized with a peptide that recognizes apoptotic cells and with organic fluorophores were characterized by several physicochemical and biological methods such as HPLC, relaxometry and photon correlation spectroscopy, which attested to their potential as bimodal tracers detected by optical imaging and MRI. An increase of relaxivity and stability of AGuIX nanoparticles is also observed after their vectorization. The biological efficiency of this novel bimodal probe to target apoptotic cells was evaluated by fluorescence microscopy, relaxometry, MRI and flow cytometry on a lymphoblastic human T-cell line. *In vitro* cell apoptosis was chemically induced by incubation with camptothecin. Our *in vitro* experiments showed a significant specificity of vectorized AGuIX nanoparticles for camptothecin-treated cells that suggests their potential efficiency as probes to target apoptosis. Copyright © 2016 John Wiley & Sons, Ltd.

Additional supporting information may be found in the online version of this article at the publisher's web site.

Keywords: nanoparticles; AGuIX; paramagnetic; fluorescence; apoptosis; MRI; imaging

1. INTRODUCTION

During recent years, outstanding research has led to the synthesis of more efficient contrast agents for pre-clinical imaging. Paramagnetic AGuIX nanoparticles are one of these new probes for medical applications (1). These paramagnetic ultrasmall rigid platforms (SRPs) have the peculiarity to include on their surface several functions allowing coupling reactions with different compounds (MRI contrast agents, fluorophores, chelators for labelling by radioisotopes, biological vectors, ...). Therefore, AGuIX nanoparticles appear as a possible multimodal nanoplatform, with the possibility to combine molecules and allow their detection by several imaging techniques such as magnetic resonance imaging (MRI), optical imaging or therapeutic applications such as radiosensitization or photodynamic therapy (2,3).

Paramagnetic AGuIX nanoparticles are composed by a polysiloxane network synthesized from hydrolysis condensation of tetraethylorthosilicate (TEOS, 40%) and aminopropyltriethoxysilane (APTES, 60%). APTES allows the presence of some amine functions as potential coupling sites for Gd-DOTA derivatives. Potentiometric titrations showed that Gd^{III} ions are strongly chelated to DOTA compounds (complexation constant $\log \beta_{110} = 24.78$ (4), very close to that of DOTAREM[®], $\log \beta_{110} = 25.58$).

Proton relaxation measurements of AGuIX suspensions have shown a high longitudinal relaxivity¹ of $11.9 \text{ s}^{-1} \text{ mM}^{-1}$ of Gd at

60 MHz and 37 °C. Moreover, they have an excellent biocompatibility, with a low cytotoxicity confirmed by cellular tests (1,4). Because of their small hydrodynamic diameter (<5 nm), they are easily excreted via the renal system. In fact, injection of mice with different Gd³⁺ concentrations of AGuIX has already allowed observation of its accumulation in kidneys 5 min after

* Correspondence to: Mario Dentamaro and Sophie Laurent, CMMI – Center for Microscopy and Molecular Imaging, Gosselies, Belgium. E-mail mario.dentamaro@gmail.com; sophie.laurent@umons.ac.be

a M. Dentamaro, L. Vander Elst, S. Montante, C. Burtea, R. N. Muller, S. Laurent Mons, Belgium

b M. Dentamaro, F. Lux, O. Tillement Villeurbanne, France

c M. Dentamaro, L. Vander Elst, R. N. Muller, S. Laurent Gosselies, Belgium

d N. Dauguet Brussels, Belgium

e A. Moussaron Villeurbanne, France

¹The relaxivity is defined as the relaxation rate enhancement induced by 1 mmol per litre of paramagnetic centre.

administration, while in bladder and urine AGuIX nanoparticles were detected 25 min post-injection (5).

Owing to the high Z -number of the gadolinium element ($Z = 64$), the nanoparticles also have a radiosensitizing effect for radiology used for cancer treatment. Multifunctional polysiloxane-based nanoparticles are thus also efficient as theranostic platforms combining imaging and therapy (1,4,6–8). Radiation therapy studies performed on tumoral cells (9,10) have shown an amplification of X-ray effects when the irradiation is performed in the presence of nanoparticles. This was also confirmed under different types of irradiation such as hadrontherapy experiments (11).

Tumour targeting is a real challenge in clinical research. AGuIX nanoparticles can be sufficiently large to prevent their extravasation from normal vessels of healthy tissues and small enough for passive accumulation within solid tumours by the EPR (enhanced permeation and retention) effect (4,12). This effect is a result of the combination between an increased tumour blood vessel permeability and a decreased rate of clearance caused by the absence of functional lymphatic vessels in the tumour (13,14). However, an active targeting is also possible by conjugating AGuIX with a vector specific to cancer cell receptors.

Our research group has previously described the functionalization of AGuIX nanoparticles with various ligands for the targeting of tumours. These markers have been grafted on free carboxylic functions of uncomplexed DOTA derivatives covalently coupled at the surface of nanoparticles (15). We have shown that grafted AGuIX is for example able to target, with a high efficiency, tumours overexpressing $\alpha_v\beta_3$ -integrins using cyclic RGD as a specific peptide (16), or extracellular melanin pigment, present in melanoma cancer environment, using quinoxaline derivatives (17). Otherwise, grafted AGuIX has also been labelled with the fluorophore cyanine 5.5 (Cy5.5), which gives bimodality properties with potential diagnostic applications by MRI and optical imaging (16).

In the present study, we focused on grafted AGuIX nanoparticles as a multimodal probe for apoptotic cell detection. Apoptosis is a programmed cell death process. It is considered as a vital

component of various processes including normal cell turnover and also the proper development and regulation of the immune system (18). In contrast to necrosis, an uncontrolled and passive process of cell death, apoptosis is an active and genetically controlled process, which does not lead to an inflammatory process as caused in necrosis by the loss of membrane cell integrity (19). The aim of this targeting is the diagnosis of pathologies associated with an excessive or an insufficient triggering of apoptosis, such as atherosclerosis, ischemia, chronic inflammation, autoimmune disorders, transplant rejection, neurodegenerative disorders, acquired immuno-deficiency syndrome (AIDS) and diabetes mellitus (20,21). Apoptosis is also associated with cancer. Indeed, cancer cells are characterized by the development of several anti-apoptotic mechanisms, which allow them to escape from their programmed death and contribute to their uncontrolled proliferation (22). Most processes in cancer therapy are based on the reactivation of cell death programs, such as apoptosis, on malignant cells (23). Radiotherapy is one of the most local treatments against solid tumours inducing cell apoptosis, but is limited by cell resistance and toxicity on peripheral healthy tissues. Therefore, targeting apoptosis represents a potential interest to observe the efficiency of a cancer treatment on tumours (24) and also to quantify the radiation-induced apoptosis on peripheral normal tissues after radiotherapy (25).

Apoptosis mechanisms can be classified into two energy-dependent pathways: the extrinsic or death receptor pathway and the intrinsic pathway or mitochondrial pathway (18). These two pathways lead to DNA fragmentation, degradation of cytoskeletal and nuclear proteins, crosslinking of proteins, formation of apoptotic bodies associated with cell membrane blebbing and externalization of phosphatidylserine phospholipid and of ligands for phagocytic cell receptors (Fig. 1).

TLVSSL (E3) peptide was identified by phage display technology as having a high affinity for phosphatidylserine, with a K_a of about $2.5 \times 10^6 \text{ M}^{-1}$, evaluated by the ELISA method (26,27). This peptide was grafted on AGuIX nanoparticles previously

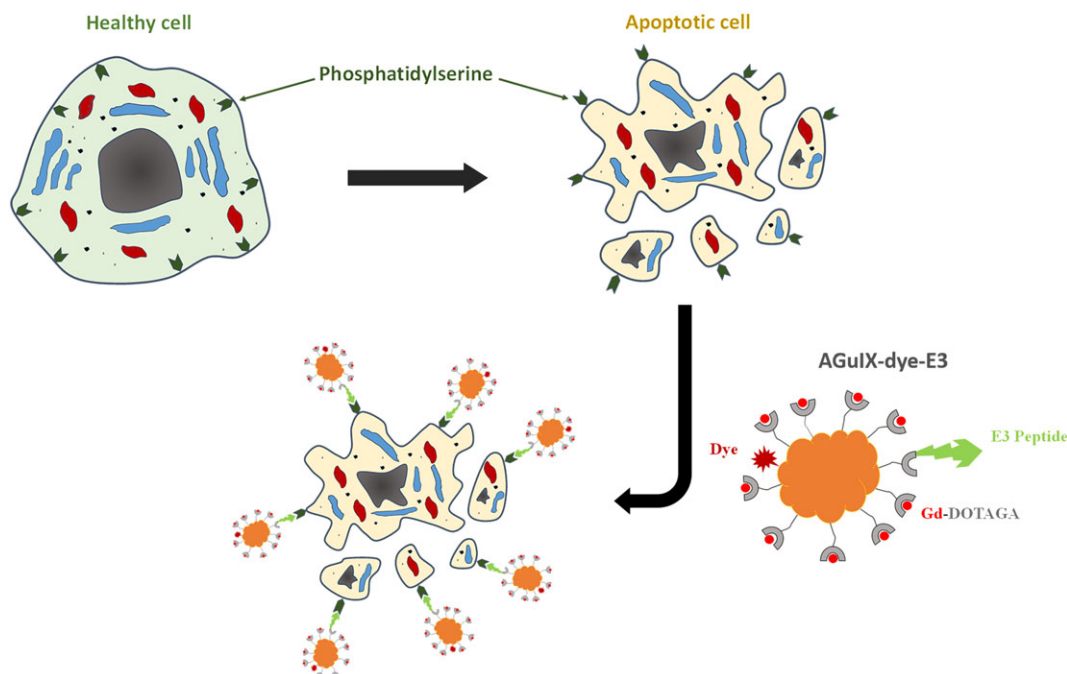


Figure 1. Schematic illustration of apoptotic cell formation, with the exposure of phosphatidylserine, and targeting by AGuIX-dye-E3 nanoparticles.

labelled with a fluorescent dye (Cy5.5 or rhodamine) to obtain an efficient bimodal probe to target apoptotic cells. Platforms were also grafted in the same conditions with the scramble SVSLLT peptide. Van Koninckxloo *et al.* (28) showed that the K_a of SVSLLT peptide is 28 times lower than the K_a of TLVSSL peptide on a micellar model exposing phosphatidylserine.

This research has been focussed on the chemical synthesis and then the physico-chemical and biological characterizations of different types of grafted AGuIX nanoparticle. Nanoparticle size and relaxivity measurements were made to confirm the peptide grafting. Their efficiency as a new contrast agent to target apoptosis has been evaluated using an *in vitro* test on a lymphoblastic human T-cell line.

2. MATERIALS AND METHODS

2.1. Synthesis

2.1.1. Materials and chemicals

N-(3-dimethylaminopropyl)-N'-ethylcarbodiimide hydrochloride (EDC, 98.0%), core-shell nanoparticles (gadolinium oxide core and polysiloxane shell) were purchased from Nano-H (Saint-Quentin-Fallavier, France). Gadolinium hydroxide hexahydrate ($\text{GdCl}_3 \cdot 6\text{H}_2\text{O}$, 99%), sodium hydroxide (NaOH, 99%), hydrochloric acid (HCl, 36.5–38%), dimethylsulfoxide (DMSO, >99.5%), dimethylformamide (DMF, >99.8%) acetonitrile (CH_3CN , >99.9%), 4-(2-hydroxyethyl)piperazine-1-ethanesulfonic acid (HEPES, >99.5%), sodium chloride (NaCl, >99.5%), trifluoroacetic acid (TFA, >99%), calcium chloride hexahydrate ($\text{CaCl}_2 \cdot 6\text{H}_2\text{O}$), Chelex® 100 sodium form and rhodamine B isothiocyanate (RITC, mixed isomers) were provided by Sigma Aldrich Chemical. Nitric acid (HNO_3 , 67%) was purchased from Merck Belgium. Cyanine 5.5 (mono-reactive NHS ester) was provided by GE Healthcare. The TLVSSL peptide (abbreviated E3) was purchased from GeneCust Luxembourg. E3 scramble (SVSLLT), 8-amino-3,6-dioxatanoil-7-TLVSSL (L-E3) and 8-amino-3,6-dioxatanoil-7-SVSLLT (L-E3Scramble) were purchased from PolyPeptide Laboratories Group (Strasbourg, France). The anhydrous DOTAGA (1,4,7,10-tetraazacyclododecane-1-glutaric anhydride-4,7,10-triacetic acid) chelate was purchased from CheMatech (Dijon, France). The Vivaspin membranes (MWCO = 5 kDa) for tangential filtration of nanoparticles were purchased from Sartorius Stedim Biotech (France).

The synthesis of the core-shell nanoparticles (core gadolinium oxide and shell polysiloxane) in diethylene glycol (DEG) has been previously described by the present authors (29).

2.1.2. Hydrolysis and complexation of anhydrous DOTAGA

AGuIX nanoparticles contain Gd-DOTAGA ligands on their surface as described previously. In order to compare relaxometric properties of AGuIX nanoparticles with a small Gd^{3+} complex, anhydrous DOTAGA was hydrolysed in basic aqueous solution (stirred overnight in 0.5 M NaOH solution at room temperature) and complexed adding $\text{GdCl}_3 \cdot 6\text{H}_2\text{O}$ at pH 6 to generate Gd-DOTAGA. Uncomplexed Gd^{3+} ions were eliminated using Chelex® 100 resin complex.

2.1.3. Grafting of dye

For the fluorescent labelling of AGuIX nanoparticles, two types of organic dye have been chosen, rhodamine B isothiocyanate or Cy5.5 NHS-ester. These fluorescent compounds were diluted in anhydrous DMSO (2.5 mg mL^{-1}) and added to an aqueous suspension at

approximately 100 mM of AGuIX nanoparticles. For the two kinds of coupling reaction achieved on the amine function of the AGuIX surface, the pH was in the range of 5–6. Cyanine 5.5 was added with a Cy 5.5/ Gd^{3+} molar ratio of 1/700, and rhodamine was added with an RITC/ Gd^{3+} molar ratio of 1/100.

RITC has been chosen to detect grafted AGuIX nanoparticles and evaluate their specificity in *in vitro* experiments. Otherwise, due to a near-infrared fluorescence emission, Cy5.5 has been functionalized to characterize labelled-nanoparticles for further *in vivo* experiments.

2.1.4. Grafting of peptides

2.1.4.1. Peptide grafting on nanoparticles without fluorophore.

First, two equivalents of EDC were added to an AGuIX suspension at pH 5 to activate carboxylic functions on the nanoparticle surface. Peptides (E3, L-E3, E3Scramble, L-E3Scramble) were previously dissolved in a 50:50 DMF/Milli-Q water mixture (135 mM) and were added 30 min after EDC activation on the AGuIX suspension. A ratio of 0.4 peptide/ Gd^{3+} at pH 7 was used. The suspension was stirred overnight.

2.1.4.2. Peptide grafting on bimodal nanoparticles. Peptides were grafted after the dye labelling. Two equivalents of EDC were added first to unpurified dye-labelled AGuIX suspension to activate carboxylic functions on the surface. Peptides were previously dissolved in a 50:50 DMF/Milli-Q water mixture (135 mM) and were added 30 min after EDC activation on dye-labelled AGuIX suspension. A ratio of 0.4 peptide/Gd was used.

2.1.5. AGuIX purification

After the grafting, suspensions were purified by ultrafiltration with Vivaspin® (Sartorius, 5 kDa polyethersulfone membrane) tubes, and finally freeze-dried.

2.2. Nanoparticle characterization

2.2.1. Proton relaxation time analysis

Longitudinal (T_1) and transverse (T_2) relaxation times were measured at 310 K using Bruker minispec (Bruker, Karlsruhe, Germany) (MQ20 (20 MHz, 0.47 T) and MQ60 (60 MHz, 1.4 T)) nuclear magnetic resonance analysers. Measurements of longitudinal and transversal relaxation times at 300 and 500 MHz were carried out using Avance 300 and Avance 500 spectrometers (Bruker, Ettlingen, Germany).

These values allow us to determine relaxation rates and relaxivities of the contrast agent:

$$R_{1,2}^{\text{obs}} = \frac{1}{T_{1,2}^{\text{obs}}} \quad (1)$$

$$r_{1,2} = \frac{R_{1,2}^{\text{obs}} - R_{1,2}^{\text{dia}}}{c} \quad (2)$$

$R_{1,2}^{\text{obs}}$ is the observed longitudinal or transverse proton relaxation rate of a solution containing the contrast agent. $R_{1,2}^{\text{dia}}$ is the diamagnetic longitudinal or transverse proton relaxation of a water solution in the absence of contrast agent. The concentration of AGuIX nanoparticles (c) is expressed in mmol L^{-1} of gadolinium.

2.2.2. Proton nuclear magnetic relaxation dispersion (NMRD) profiles

NMRD profiles illustrate the evolution of longitudinal relaxation rate R_1 at different magnetic fields from 0.12 mT to 1.2 T. These NMRD profiles were recorded on a fast field cycling relaxometer (Stelar, Mede, Italy) at 37 °C.

2.2.3. AGuIX synthesis and purification

A large excess of anhydrous DOTAGA (33 g) was added to the core-shell particles in DEG (1 L at 30 mM $[\text{Gd}^{3+}]$) for covalent grafting, with a ratio of two DOTAGA per Gd^{3+} . The resulting mixture was stirred for 48 h at room temperature. The nanoparticles were then precipitated in acetone (3 L). Acetone was removed and the nanoparticles were washed two more times in acetone (1.5 L). The nanoparticles were then dispersed in water (500 mL). An aqueous solution of DTPA 120 mM (500 mL) was added to the nanoparticle dispersion. Finally, the remaining acetone was evaporated at 37 °C overnight. Purification of the nanoparticles was performed by filtration through Vivaspine membranes (MWCO = 5 kDa). The colloidal solution was introduced into 20 mL Vivaspine tubes, and centrifuged. This step was repeated several times, by filling the tube with water (V_i) and centrifuging to a final volume (V_f), until a purification rate (Pr) of 22 000 was obtained. Pr was calculated according to

$$Pr = \frac{V_{i1} V_{i2} \dots V_{in}}{V_{f1} V_{f2} \dots V_{fi}} \quad (3)$$

Then, the solution was filtered through 0.2 mm syringe filters to remove the largest impurities. The solution was freeze-dried for storage, using a Christ Alpha 1-2 lyophilizer.

2.2.4. Measurements of the gadolinium content in AGuIX nanoparticles

2.2.4.1. Developed protocol for AGuIX nanoparticles displaying non-complexed DOTA-like ligands. To 20 μL of AGuIX suspension in water, 80 μL of KOH (2 M) was added. After 4 h, 200 μL of nitric acid (67%) and 100 μL of H_2O_2 (30%) were added and the solution was kept at room temperature for 48 h. Longitudinal relaxation time T_1 was directly recorded in the acidic suspension at 37 °C and 60 MHz. The measured relaxation time allowed us to determine a synthesis yield of 60% of gadolinium.

2.2.4.2. Developed protocol for functionalized AGuIX nanoparticles. To determine the concentration of nanoparticle suspension in equivalent of gadolinium ions, the suspension was diluted with one equivalent volume of nitric acid 67% and heated overnight at 75 °C.

These chemical processes allow the destruction of nanoparticles and the decomplexation of gadolinium ions from DOTA. The relaxation rate measured for the acidic suspension is directly proportional to the concentration of free gadolinium.

2.2.5. Fluorescence measurements

2.2.5.1. Measurement of non-complexed DOTA-like ligands by fluorescence titration. Fluorescence measurements were carried out using a Varian Cary Eclipse fluorescence spectrophotometer, in the resolved time mode. The parameters used were 395 nm

excitation wavelength, which is a characteristic excitation for Eu^{3+} ions, excitation slit 10 nm, emission slit 10 nm, delay time 0.1 ms and gate time 5 ms.

2.2.5.2. Fluorescence properties of labelled AGuIX. Fluorescence properties of labelled AGuIX nanoparticles were obtained by absorption and emission spectrum obtained with a LS55 fluorescence spectrometer (PerkinElmer, Waltham, MA, USA). The parameters used for Cy5.5-labelled AGuIX were 679 nm excitation wavelength, excitation slit 4 nm and emission slit 5 nm. The parameters used for RITC-labelled AGuIX were 570 nm excitation wavelength, excitation slit 2.5 nm and emission slit 2.5 nm.

2.2.6. High performance liquid chromatography (HPLC)

Gradient HPLC analysis was carried out using the Shimadzu Prominence series UFLC system equipped with a CBM-20A controller bus module, an LC-20 AD liquid chromatograph, a CTO-20A column oven, an SPD-20A UV – visible detector at 295 and 350 nm and a RF-20A fluorescence detector. Analytical RP-HPLC was performed in a Jupiter C4 column ($150 \times 4.60 \text{ mm}^2$, 5 μm , 300 Å, Phenomenex®) with a gradient mobile phase (95% Solvent A/5% Solvent B (A = Milli-Q water/TFA, 99.9/0.1 (v/v); B = ACN/Milli-Q water/TFA, 90/9.9/0.1 (v/v/v)) at a flow rate of 1 mL min^{-1} (TFA, trifluoroacetic acid; CAN, acetonitrile). Samples were subsequently eluted with an enhancement of gradient from 5% to 90% of Solvent B (in Solvent A) over 30 min; the concentration of Solvent B was maintained over 10 min followed by a decrease to 5% over a period of 10 min to re-equilibrate the system. Before the analysis of each sample, a baseline was acquired under the same conditions by loading Milli-Q water into the injection loop. The column temperature was maintained at 25 °C. A volume of 20 μL of samples was loaded at approximately 5 mM Gd concentration at pH 7.4. The AGuIX chromatogram acquired at 295 nm, which corresponds to the maximum absorption of AGuIX nanoparticles, presented a peak with a retention time of 10.2 min. The purity was 90%. The analysis of Cy5.5 systems was achieved with a fluorescence emission measured at 700 nm and an excitation at 675 nm.

2.2.7. Dynamic light scattering size measurement

The hydrodynamic diameter and size distribution of nanoparticles was estimated using the dynamic light scattering (DLS) program of photon correlation spectroscopy (PCS). Data were collected at 20 °C using a Zetasizer Zen 3600 particle size analyser with a 633 nm He-Ne laser from Malvern Instruments, UK.

For measurements, lyophilized particles were first dispersed in water for 1 h at room temperature, $[\text{Gd}^{3+}] = 100 \text{ mM}$ and $\text{pH} = 7.4$. Then particles were diluted to $[\text{Gd}^{3+}] = 2.5 \text{ mM}$ and measurements immediately made.

2.2.8. Magnetic resonance imaging

Acquisition of MRI images was performed at room temperature, on a 7 T PharmaScan 70:16 imaging system (Bruker, Ettlingen, Germany). T_1 -weighted images of contrast agent were obtained using a spin-echo sequence with the rapid acquisition with relaxation enhancement (RARE) method. Acquisition of T_2 -weighted MRI images was conducted according to a turboRARE method.

2.3. In vitro characterizations

2.3.1. Apoptotic cells

Affinity for apoptotic cells was evaluated on the Jurkat human T lymphocyte cell line. Cells were cultured in RPMI medium 1640 (Gibco®, Life Technologies, Gent, Belgium) supplemented with 10% of foetal bovine serum (FBS, Gibco®, Life Technologies) and 1% penicillin–streptomycin (Pen Strep, Gibco®, Life Technologies). Apoptosis was induced by the incubation of Jurkat cells with camptothecin (MP Biomedicals, Brussels, Belgium). The apoptosis targeting efficiency of grafted AGuIX nanoparticles was evaluated using fluorescence microscopy and relaxometry measurements on Jurkat cells treated with 2 μM of camptothecin over 24 h.

2.3.1.1. In vitro characterization of targeting efficiency. Treated and control cells were resuspended in fresh culture medium. After centrifugation (4500 rpm, 15 min), the apoptosis induction rate was evaluated using an annexin V apoptosis detection kit (FITC–annexin V, propidium iodide (PI), Sigma Aldrich Chemicals) on 5×10^5 cells at the concentration of 10^6 cells mL^{-1} in Ca^{2+} buffer containing 20 μL of 2 $\mu\text{g mL}^{-1}$ Hoechst 33342 trihydrochloride (Life Technologies) to stain the DNA of cells. PI was used to stain the DNA of necrotic and late apoptotic state cells.

2.3.2. Evaluation of apoptotic cells targeting efficiency by fluorescence microscopy

Control and apoptotic cells were incubated with nanoparticles for 2 h at room temperature under mechanical stirring at a gadolinium concentration of 0.8 mmol L^{-1} in nanoparticles. Grafted

and labelled AGuIX nanoparticles were added to 4×10^6 cells at the concentration of 2×10^6 cells mL^{-1} . Subsequently, the cells were centrifuged (4500 rpm, 15 min) and rinsed three times with 2 mL of Ca^{2+} buffer (2.5 mM CaCl_2 ; 150 mM NaCl; 10 mM HEPES; pH 7.4). Then, cell pellets were suspended in 25 μL of mounting medium for fluorescence with DAPI (VECTASHIELD®, Vector Laboratories, Labconsult, Brussels, Belgium). Cell pictures were taken with a DM2000 Leica microscope equipped with a DFC 425C camera (Leica Microsystems, Groot-Bijgaarden, Belgium). Experiments were performed in triplicate.

2.3.3. Evaluation of apoptotic cells targeting efficiency by relaxometry and MRI

Control and apoptotic cells were incubated with nanoparticles for 2 h at room temperature under mechanical stirring with a gadolinium concentration of 4 mmol L^{-1} in nanoparticles. Grafted and labelled AGuIX nanoparticles were added to 10^7 cells at the concentration of 2×10^6 cells mL^{-1} . Thereafter, the cells were centrifuged (4500 rpm, 15 min) and rinsed three times with 3 mL of Ca^{2+} buffer (2.5 mM CaCl_2 ; 150 mM NaCl; 10 mM HEPES; pH 7.4). Then, cell pellets were suspended in 80 μL of gelatin (Sigma Aldrich, Diegem, Belgium) previously dissolved in Ca^{2+} buffer. Longitudinal relaxation times of suspended cell pellets were acquired with the MQ60 minispec instrument at 15 °C. T_1 -weighted images and T_1 measurements of pellets were also obtained with a PharmaScan 7 T MRI scanner.

2.3.4. Flow cytometry

The specificity of grafted AGuIX nanoparticles for apoptotic cells was also evaluated using a LSRFortessa flow cytometer (BD

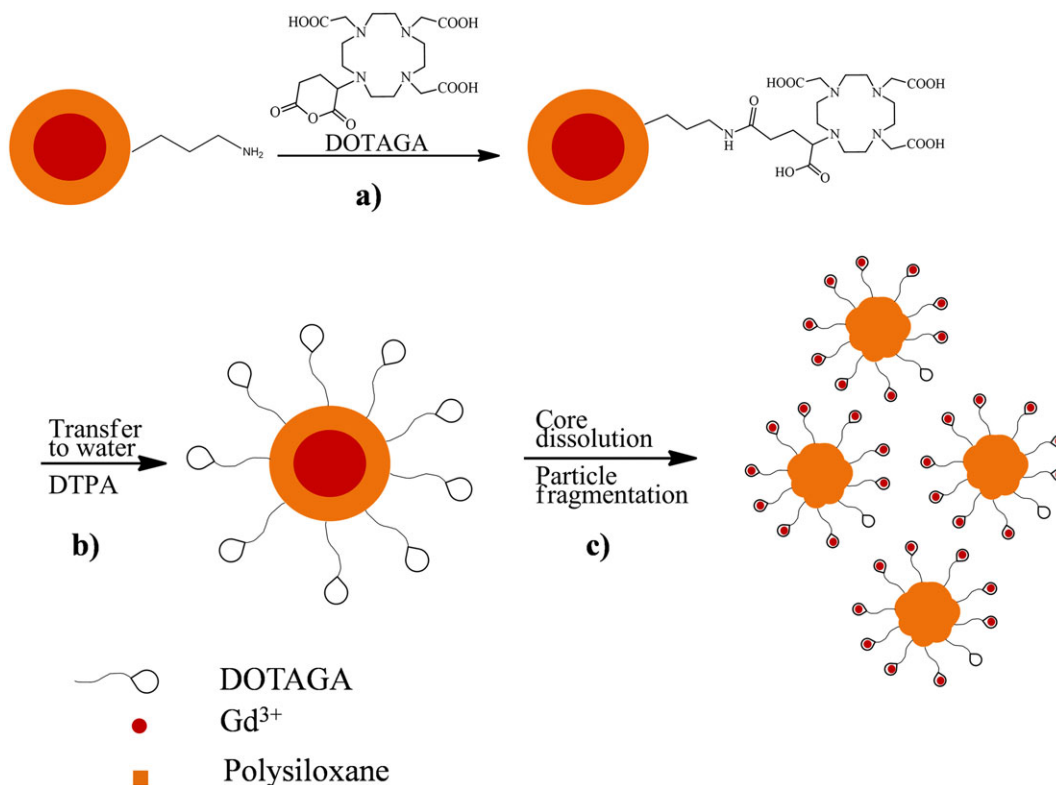


Figure 2. Preparation of AGuIX: (a) DOTAGA grafting, (b) transfer to water and addition of DTPA and (c) core dissolution and polysiloxane fragmentation.

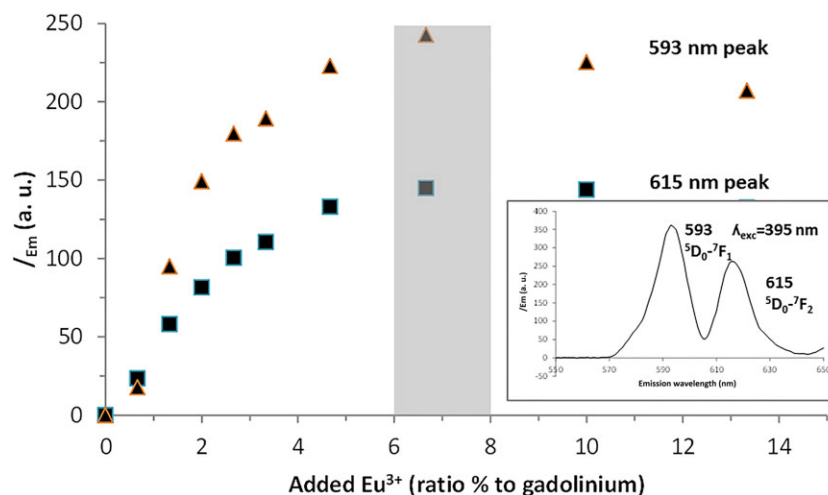


Figure 3. Quantification of the ratio of non-complexed DOTA-like ligands by time-resolved luminescence with a time delay of 0.2 ms. The intensities of $^5D_0-^7F_1$ (squares) and $^5D_0-^7F_2$ (triangles) transition peaks are plotted as a function of increasing amounts of Eu^{3+} .

Biosciences, Franklin Lakes, NJ, USA). Analyses were performed on Jurkat cells previously treated with camptothecin and incubated with grafted and labelled AGuIX. Before each experiment, cells (3×10^5 in 200 μ L of Ca^{2+} buffer) were stained with 10 μ L of 7-amino-actinomycin (7-AAD 0.05 mg mL $^{-1}$, Life Technologies) and 5 μ L of FITC-annexin V (25 μ g mL $^{-1}$, BD Pharmingen). 7-AAD is known to target effectively the DNA of dead and late apoptotic state cells. Annexin V is a large protein known to target phosphatidylserine on cell membranes at the early stage of apoptosis. RITC-labelled AGuIX nanoparticles were detected using a yellow-green (561 nm) laser for excitation with a BP 582/15 nm filter for emission. Experiments were performed in triplicate.

3. RESULTS AND DISCUSSION

3.1. Nanoparticle synthesis

The gadolinium oxide core, the polysiloxane shell, with a ratio of 4:1 for Si:Gd, and the grafting of DOTAGA onto the amine functions of the core-shell particles, were prepared in diethylene glycol (DEG) according to our previously reported strategy (4,30).

The DOTA-like ligands were grafted using anhydrous DOTAGA through amide bonds between amine functions on nanoparticles and glutaric anhydride on DOTAGA (Fig. 2(a)).

The particles were then transferred to water. The core dissolution leads to fragmentation of the polysiloxane shell into ultra-small rigid platforms (USRPs) of polysiloxane, as previously demonstrated with DTPA and DOTA derivatives (1,4). The resulting Gd^{3+} from the core dissolution was chelated by DOTA-like ligands. In order to eliminate some of the Gd^{3+} and to keep some non-complexed ligands on the surface, these USRPs were then treated with DTPA solution (Fig. 2(b), (c)). DTPA, Gd -DTPA, unreacted reagents and the smallest nanoparticles were then removed by tangential filtration using 5 kDa cut-off membranes. After the purification, the USRPs, also called AGuIX nanoparticles, were freeze-dried for storage. They were dispersed again in water before use, and the hydrodynamic diameter obtained after dispersion is equal to the diameter before freeze-drying (about 1.8 nm).

The quantification of the ratio of non-complexed DOTA-like ligands was determined by Eu^{3+} time-resolved luminescence.

3.2. Measurement of non-complexed DOTA-like ligands by fluorescence titration

To obtain the quantitative proportion of non-complexed DOTA-like ligands, time-resolved luminescence experiments were performed after addition of europium cations in a solution containing USRPs. It is possible to differentiate the free ligands from the complexed ones, since only the first are able to chelate additional europium cations. This chelation can be easily followed by the correlative change in the europium luminescence. Indeed, free europium cations have a luminescence almost completely quenched by the OH oscillators present in water, whereas the complexed Eu^{3+} are preserved from quenching by the protecting surrounding ligand. Several sets were prepared by addition of different amounts of europium cations to the nanoparticles, ranging from zero to one times the gadolinium content. That is, europium chloride ($EuCl_3 \cdot 6H_2O$) was dissolved in water, and added to the nanoparticle solutions. Because of the H^+ release during rare earth complexation, the pH of the solutions was adjusted to 6, which is high enough for fast gadolinium complexation, but simultaneously low enough to prevent hydroxide formation. The mixtures were heated for 48 h at 80 $^{\circ}C$. Luminescence measurements were made in water solutions containing 15 mM of gadolinium. Eu^{3+} cations were excited at 395 nm, which permits us to obtain two emission peaks: $^5D_0-^7F_1$ at 593 nm and $^5D_0-^7F_2$ at 615 nm.

For small amounts of added Eu^{3+} (<6% per gadolinium), the intensity of both emission peaks increases with the amount of

Table 1. Hydrodynamic diameter study of synthesized AGuIX nanoparticles

	HD (nm)
AGuIX	2.7 ± 0.7
AGuIX-E3	4.0 ± 1.2
AGuIX-RITC	4.5 ± 2.1
AGuIX-RITC-E3	5.1 ± 1.9
AGuIX-L-E3	3.8 ± 1.4
AGuIX-RITC-L-E3	3.9 ± 1.3

Table 2. Relaxivity values, at 20 MHz and 60 MHz, of AGuIX nanoparticles at 2 mM [Gd³⁺], measured 5 min after dilution

	AGuIX	AGuIX–E3	AGuIX–E3Sc	AGuIX–L-E3	AGuIX–L-E3Sc	AGuIX–Cy5.5	AGuIX–Cy5.5–E3	AGuIX–RITC	AGuIX–RITC–E3	AGuIX–RITC–E3Sc	AGuIX–RITC–L-E3
r_1 (s ^{−1} mM ^{−1}) (37 °C, 20 MHz)	7.8	12.7	13.0	18.2	18.4	13.0	13.1	12.9	16.1	14.1	17.7
r_2 (s ^{−1} mM ^{−1}) (37 °C, 20 MHz)	8.7	14.7	14.6	20.8	21.1	13.8	14.0	13.9	17.4	/	20.7
r_2/r_1 (20 MHz)	1.1	1.1	1.1	1.1	1.1	1.1	1.1	1.1	1.1	/	1.2
r_1 (s ^{−1} mM ^{−1}) (37 °C, 60 MHz)	6.9	10.3	10.6	15.2	15.4	11.6	11.4	11.2	12.1	12.1	15.7
r_2 (s ^{−1} mM ^{−1}) (37 °C, 60 MHz)	8.9	15.3	15.6	21.8	22.7	15.3	16.0	15.0	18.9	20.4	21.5
r_2/r_1 (60 MHz)	1.3	1.5	1.5	1.4	1.5	1.3	1.4	1.3	1.6	1.7	1.4

Eu³⁺, which evidences the formation of increasing quantities of luminescent Eu³⁺ chelates. For large amounts of added Eu³⁺ (>8%), the luminescence intensity reached a plateau (Fig. 3), the additional Eu³⁺ remaining free (thus non-luminescent) in solution. Therefore we can evaluate the ratio of non-complexed DOTA-like ligands as 7% ± 1% of the amount of gadolinium present in the particles.

3.3. Dye and peptide grafting

Peptide-grafted AGuIX was synthesized by the formation of amide bonds between free carboxylic functions of AGuIX and N-terminal functions of the peptide using the coupling agent EDC. AGuIX nanoparticles have approximately 10 Gd³⁺ ions complexed on their surface. A grafting rate of 0.4 peptide/Gd has been chosen, corresponding to a ratio of 4 peptides per nanoparticle, which is an excess ratio considering that the platform has around one fixation site. To increase the peptide mobility, AGuIX was also grafted with peptides bound to a linker through an amide bond with 8-amino-3,6-dioxaoctanoic acid. For dye-labelled nanoparticles, RITC or Cy5.5 was grafted on the amine function on the AGuIX surface by thiourea bonds for RITC and by amide bonds for Cy5.5. Some of these particles were further grafted with peptides (AGuIX–RITC–E3, AGuIX–RITC–L-E3, AGuIX–RITC–E3Sc, AGuIX–RITC–L-E3Sc, AGuIX or AGuIX–Cy5.5).

3.4. Grafted AGuIX physical characterizations

DLS analyses performed on 10 mM suspensions showed an increase of hydrodynamic diameter after the grafting of AGuIX nanoparticles with RITC, the peptide or both (Table 1 and Fig. S1 in supporting information). AGuIX labelled with Cy5.5 could not be analysed by DLS due to the high fluorescence absorbance at the wavelength of the laser source (633 nm).

The grafting of the peptide is thus confirmed by the enhancement of the hydrodynamic diameter measured with PCS. Moreover, an increase of nanoparticle size is also observed with HPLC through the increase of the retention time of AGuIX–Cy5.5–E3 suspensions eluted into a column (Fig. S4 in supporting information). The UV–visible absorption detector was fixed at 295 nm, a wavelength specific to each type of AGuIX nanoparticle. Chromatograms showed different retention times: 10 min for AGuIX nanoparticles, 11 min for AGuIX–Cy5.5 and finally 12.5 min for AGuIX–Cy5.5–E3. AGuIX–Cy5.5–E3 nanoparticles were detected at the same time on both detectors (UV and

fluorescence), which confirmed the functionalizations by Cy5.5 dye and by the peptide.

Measurements of relaxation rates give indications of the efficiency of these gadolinium-based MRI contrast agents. Longitudinal (r_1) and transverse (r_2) relaxivities (Table 2) were measured. These relaxivities have been obtained by a measurement of relaxation times 5 min after the dilution of AGuIX nanoparticles at 2 mM [Gd³⁺] in HEPES buffer at pH 7.4.

These measurements indicate an enhancement of transverse and longitudinal relaxivities for AGuIX nanoparticles after their grafting. NMRD profiles performed on 4 mM suspensions, 10 min after their dilutions, showed a proton relaxation enhancement (PRE) at all magnetic fields (Fig. 4). Moreover, at clinical MRI frequencies (6–130 MHz), the PRE for functionalized AGuIX nanoparticles is quite high. This increase is usually explained by an increase in the rotational correlation time (τ_R) of the paramagnetic complex (31,32). Table 3 shows the relaxivity values for AGuIX nanoparticles measured at 300 and 500 MHz on more concentrated solutions (>20 mM) to minimize degradation. As expected, the ratios r_2/r_1 of the grafted nanoparticles increase markedly, confirming the larger size after grafting.

The NMRD profiles of AGuIX have been compared with the profile of a small Gd³⁺ complex, Gd-DOTAGA. As expected, the relaxivities of all AGuIX particles are larger than those of Gd-DOTAGA over the whole frequency range. The fittings of the NMRD data were performed using the Solomon–Bloembergen–Morgan (SBM) model for the inner-sphere contribution and the Freed model for the outer-sphere contribution (33,34). This classical analysis of the NMRD profile is known to be inadequate for the low field data of nanosized systems. In accordance with a well established approach (35–38), the data at magnetic fields lower than 3 MHz were thus not included in the fittings. Table 4 summarizes the parameters obtained from the fittings of the profiles. For Gd-DOTAGA, the fitting was performed with the usual inner-sphere and outer-sphere contributions with the following parameters: $r = 0.31$ nm; $d = 0.36$ nm; $D = 3.3 \times 10^{-9}$ m² s^{−1} (39); $\tau_M = 116$ ns as determined by the analysis of the ¹⁷O transverse relaxation rates as a function of the temperature (40) (Fig. S7 in supporting information); $q = 1$; $\tau_R = 69 \pm 6.7$ ps, $\tau_{SO} = 301 \pm 89$ ps and $\tau_V = 3.9 \pm 1.4$ ps at 310 K. These values agree quite well with those reported by F. Kielar *et al.* (38), except for the value of τ_M , which is slightly larger in our study.

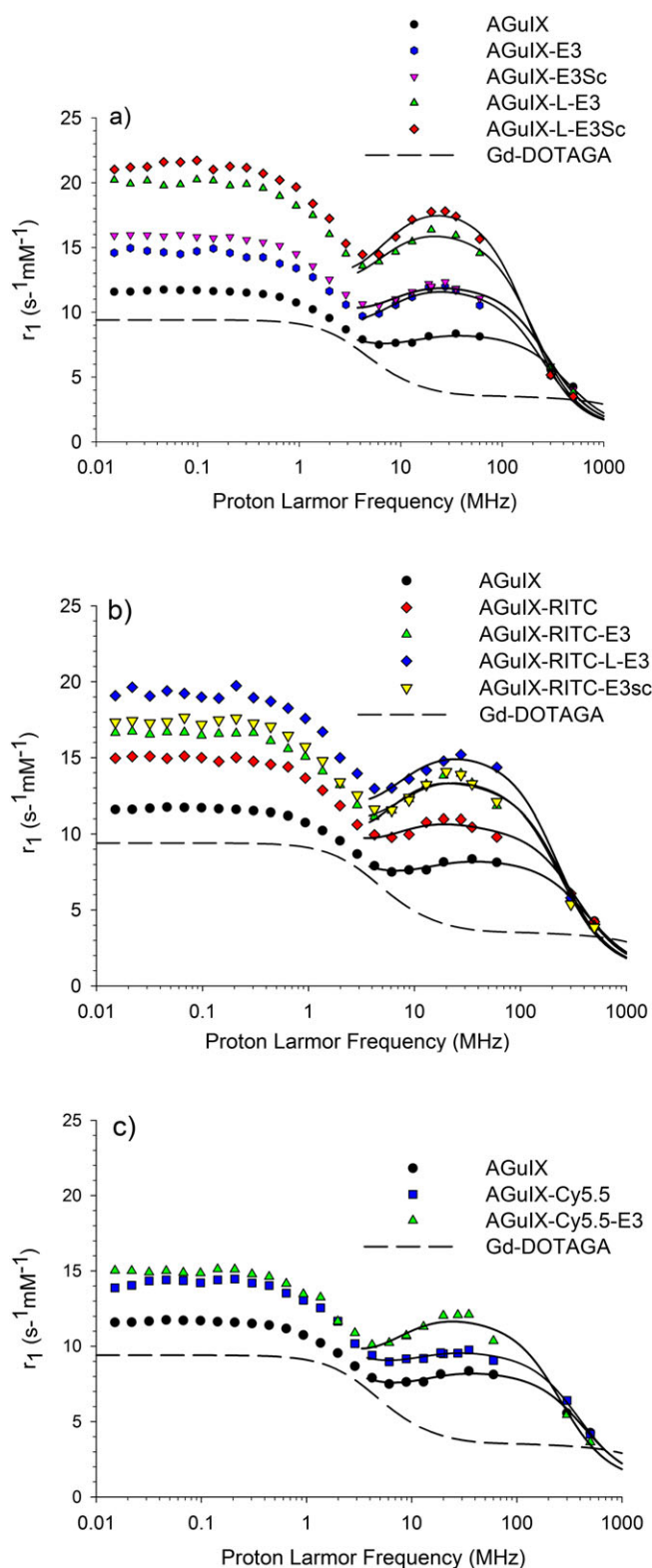


Figure 4. NMRD profiles of grafted AGuIX nanoparticles suspended at 4 mM $[Gd^{3+}]$ in water and measured 10 min after dilution and compared with non-grafted AGuIX and Gd-DOTAGA. (a) NMRD profiles of each kind of non-labelled nanoparticle. (b) NMRD profiles of each kind of nanoparticle labelled with RITC. (c) NMRD profiles of each kind of synthesized AGuIX nanoparticle labelled with Cy5.5.

As shown by the data of Table 4, the water residence times obtained are markedly larger than for Gd-DOTAGA. This type of behaviour has already been reported by F. Kielar *et al.* (38) for paramagnetic lipid nanoparticles made of Gd-DOTAGA lipophilic derivatives inserted in liposomes. However, this increase of the water residence time is lower when a spacer is present (AGuIX-L-E3, AGuIX-L-E3Sc and AGuIX-RITC-L-E3). The graftings of both fluorophores result in similar NMRD profiles and have little influence on the tumbling but seem to lower slightly the water residence time as compared with AGuIX. In contrast, the grafting of the peptides results in a marked increase of the rotational correlation time. In a second approach, the Lipari-Szabo model for the description of the local rotational dynamics was included in the theoretical fittings but the quality of the fittings was not markedly increased (results not shown).

T_1 -weighted images (Fig. 5(a)) and T_2 -weighted images (Fig. 5(b)) were obtained on 4 mM $[Gd^{3+}]$ AGuIX suspensions at 7.4 T at room temperature. They were acquired 30 min after the AGuIX dilution. A clear positive contrast enhancement was observed for the paramagnetic AGuIX, AGuIX-E3 and AGuIX-Cy5.5-E3 nanoparticles on T_1 -weighted images.

At a magnetic field of 7 T (300 MHz), the longitudinal relaxivities of vectorized AGuIX and AGuIX nanoparticles are in the same range. This explains the quite close brightness observed for the three types of AGuIX nanoparticle. However, at this high magnetic field, the transversal relaxivity r_2 of vectorized AGuIX is markedly higher than the r_2 of non-vectorized nanoparticles (see Table 3); thereby, a more pronounced darkening can be observed on the T_2 -weighted image of the vectorized AGuIX.

3.5. AGuIX stability

As a result of the progressive degradation of the polysiloxane network, due to the hydrolysis of Si–O–Si bonds (41), the AGuIX nanoparticles are rapidly destabilized at low concentration and physiological pH. The evolution of NMRD profile versus time of AGuIX displaying non-complexed DOTA-like ligands, performed with 4 mM suspension (Fig. 6(a)), showed a global decrease of longitudinal relaxivity. Figure 6(b), (c) illustrates the AGuIX degradation by the relaxivity percentage loss with time at fixed magnetic fields (20 MHz and 60 MHz). In aqueous-buffered suspension containing 2 mM $[Gd^{3+}]$ at pH 7.4, approximately 50% of the longitudinal relaxivity at 60 MHz and 20 MHz is lost after 70 min, whereas the $r_{1,2}$ decrease of the 20 MHz solution is lower than 10%. The kinetics of degradation is thus dependent on Gd^{3+} concentration in suspension (29).

Truillet *et al.* (42) published some studies on the aging of AGuIX nanoparticles. By HPLC-MS analysis, they characterized the degraded product of AGuIX nanoparticles as siloxane fragments with Gd-DOTA-like structures. This kind of degradation can be evoked to explain the relaxometric behaviour described earlier (Fig. 6(a)–(c)). Figure 6(a) shows the decrease of r_1 of AGuIX nanoparticles. After 24 h, the high field relaxivities are similar to the r_1 of Gd-DOTAGA, indicating that the rotational correlation times are close. The lower values of r_1 at low magnetic field after 24 h can be related to changes in the electronic relaxation rate of gadolinium of the degradation products, such as a decrease of the symmetry and/or

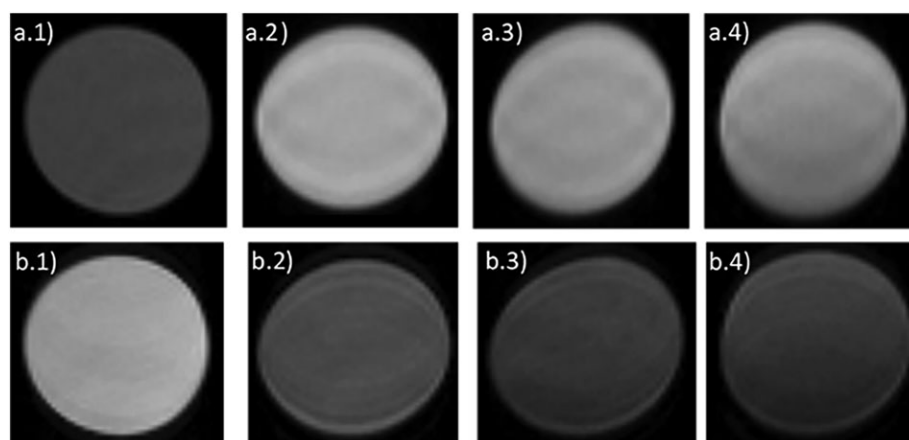
Table 3. Relaxivity values, at 300 and 500 MHz, of AGuIX nanoparticles suspended in water with highly concentrated conditions (>20 mM Gd)

	AGuIX	AGuIX–E3	AGuIX–E3Sc	AGuIX–L-E3	AGuIX–L-E3Sc	AGuIX–Cy5.5	AGuIX–Cy5.5–E3	AGuIX–RITC	AGuIX–RITC–E3	AGuIX–RITC–E3Sc	AGuIX–RITC–L-E3
r_1 ($s^{-1} \text{ mM}^{-1}$) (37 °C, 300 MHz)	5.6	5.1	5.8	5.5	5.2	6.4	5.4	6.1	5.7	5.4	5.8
r_2 ($s^{-1} \text{ mM}^{-1}$) (37 °C, 300 MHz)	11.3	18.8	17.3	19.0	16.8	22.0	17.5	15.4	23.2	18.9	18.8
r_2/r_1 (300 MHz)	2.0	3.7	3.0	3.4	3.2	3.4	3.2	2.5	4.1	3.5	3.2
r_1 ($s^{-1} \text{ mM}^{-1}$) (37 °C, 500 MHz)	4.3	5.1	4.0	3.7	3.5	4.8	3.6	4.2	4.0	3.9	3.8
r_2 ($s^{-1} \text{ mM}^{-1}$) (37 °C, 500 MHz)	10.0	21.1	17.3	20.5	16.8	21.0	19.0	15.0	22.5	21.7	18.4
r_2/r_1 (500 MHz)	2.3	4.1	4.3	5.5	4.8	4.4	5.3	3.6	5.6	5.6	4.8

Table 4. Parameter values obtained from the fittings of the NMRD profiles¹

	AGuIX	AGuIX–E3	AGuIX–E3Sc	AGuIX–L-E3	AGuIX–L-E3Sc
τ_R (ns)	0.67 ± 0.04	1.36 ± 0.05	1.01 ± 0.03	1.34 ± 0.04	1.59 ± 0.04
τ_M (ns)	1880 ± 53	1410 ± 29	1220 ± 26	847 ± 20	764 ± 16
τ_{SO} (ps)	267 ± 34	237 ± 56	382 ± 71	450 ± 72	450 ± 58
τ_V (ps)	15 ± 2	31 ± 7	24 ± 4	33 ± 2	32 ± 2
	AGuIX–RITC	AGuIX–RITC–E3	AGuIX–RITC–E3sc	AGuIX–RITC–L-E3	AGuIX–Cy5.5
τ_R (ns)	0.79 ± 0.03	1.11 ± 0.04	1.24 ± 0.04	1.20 ± 0.04	0.70 ± 0.03
τ_M (ns)	1360 ± 35	1060 ± 24	1090 ± 24	879 ± 25	1480 ± 44
τ_{SO} (ps)	352 ± 92	219 ± 94	392 ± 80	450 ± 22	450 ± 50
τ_V (ps)	28 ± 7	44 ± 14	28 ± 6	28 ± 2	15 ± 2
AGuIX–Cy5.5–E3					
τ_R (ns)	1.59 ± 0.04				
τ_M (ns)	764 ± 16				
τ_{SO} (ps)	450 ± 58				
τ_V (ps)	32 ± 2				

¹The following parameters were fixed during the fitting: distance for inner-sphere interaction, $r=0.31$ nm; distance of closest approach, $d=0.36$ nm; diffusion coefficient, $D=2.9 \times 10^{-9} \text{ m}^2 \text{ s}^{-1}$; number of water molecules in the first coordination sphere, $q=1$.

**Figure 5.** (a) T_1 -weighted images of paramagnetic AGuIX nanoparticles: (a.1) water; (a.2) AGuIX NP; (a.3) AGuIX–E3 NP; (a.4) AGuIX–Cy5.5–E3 ($TE=9.1$ ms, $TR=1300$ ms). (b) T_2 -weighted images of paramagnetic AGuIX nanoparticles: (b.1) water; (b.2) AGuIX NP; (b.3) AGuIX–E3 NP; (b.4) AGuIX–Cy5.5–E3 ($TE=33.3$ ms, $TR=2500$ ms).

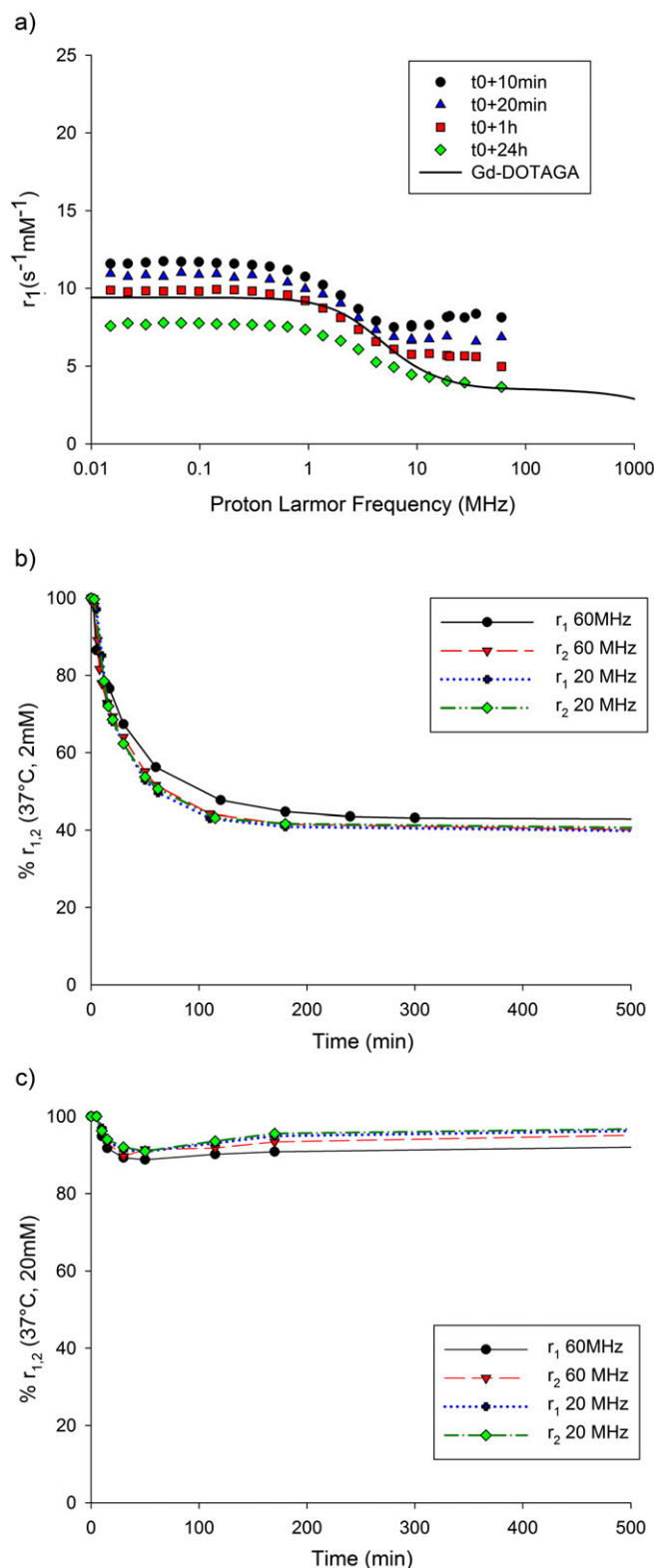


Figure 6. (a) Evolution of NMRD profiles of AGuIX nanoparticles suspended in water at 4 mM $[Gd^{3+}]$. (b) Evolution of the percentage loss of AGuIX relaxivities at fixed magnetic fields in a Ca^{2+} buffer suspension at 2 mM $[Gd^{3+}]$ and pH 7.4. (c) Evolution of the percentage loss of AGuIX relaxivities at fixed magnetic fields in a Ca^{2+} buffer suspension of 20 mM $[Gd^{3+}]$ and pH 7.4.

the rigidity of these compounds as compared with Gd-DOTAGA.

These analyses performed on grafted AGuIX nanoparticles showed an AGuIX stabilization induced by their

grafting. Indeed, the degradation kinetics is slower, with a loss of 50% of r_1 reached after approximately 300 min (Fig. 7), as compared with 70 min for AGuIX nanoparticles.

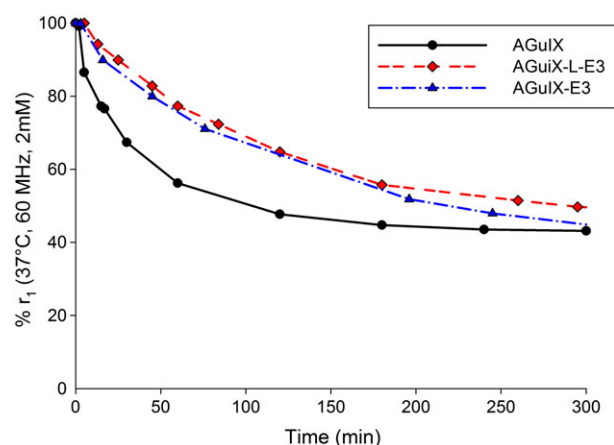


Figure 7. Evolution of the percentage loss of r_1 at 60 MHz and 37 °C of AGuIX, AGuIX-E3 and AGuIX-L-E3 in Ca^{2+} buffer at a concentration of 2 mM $[\text{Gd}^{3+}]$.

3.6. Fluorescence properties of labelled AGuIX

For further *in vivo* applications by optical imaging it is necessary to use a fluorophore with a high tissue penetration of absorbed and emitted photons (43). This can be reached using NIR (700–1000 nm) wavelengths in biomedical imaging. The organic fluorophore Cy5.5 has been chosen for its absorption and its

fluorescence emission in the near infrared range. Cy5.5 was added at an initial ratio of 1/700 Gd to obtain AGuIX nanoparticles. The dye functionalization was confirmed by the maximum intensity of absorption at 676 nm and a maximum intensity of emission at 690 nm for AGuIX–Cy5.5 and AGuIX–Cy5.5–E3 (see supporting information).

The rhodamine fluorophore was grafted with an initial ratio of 1 RITC/100 Gd. After the labelled-platform grafting, the obtained RITC/Gd ratio was estimated by fluorescence spectroscopy using a calibration curve performed with RITC solutions. This ratio was evaluated at 0.006 RITC/Gd.

3.7. Non-covalent interaction study

Human serum albumin (HSA) is a large protein known to constitute 4.5% of human plasma (44). Non-specific interactions between HSA and contrast agents will induce an extension of their blood half-life (45), increasing the time available to reach the specific target. A non-covalent binding should influence the PRE, with a change of the ‘hump’ between 9 and 60 MHz (Fig. S5 in supporting information) and could modify the rate of degradation of the nanoparticles (46). The similarity of the profiles confirmed the absence of interaction between blood plasma protein HSA and AGuIX nanoparticles with and without peptide.

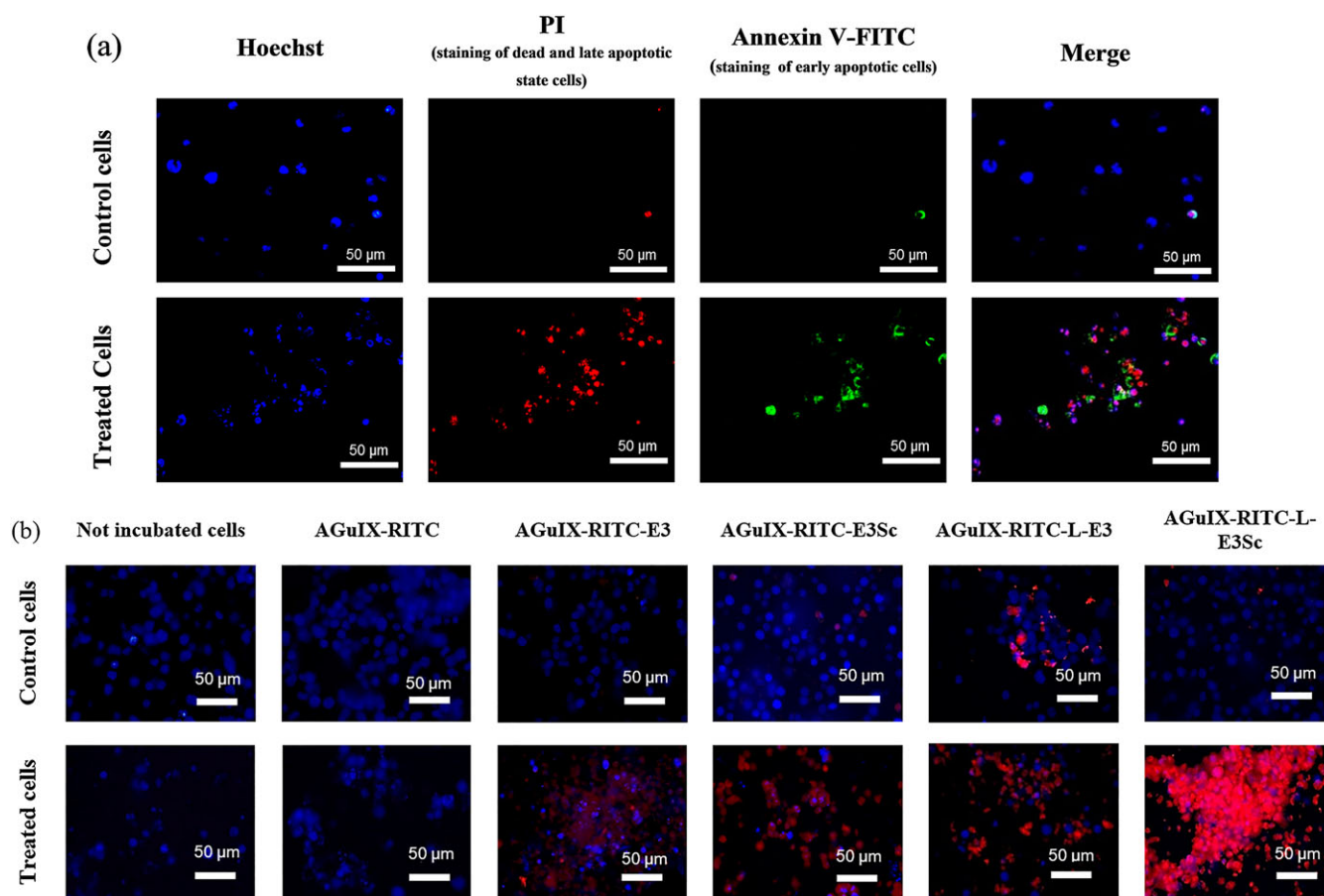


Figure 8. (a) Fluorescence microscopy of control cells and cells treated with 2 μM camptothecin for 24 h. Both cultures were stained with Hoechst, PI and annexin V-FITC. (b) Fluorescence microscopy merged images of control cells and cells treated with 2 μM camptothecin for 24 h incubated with labelled AGuIX-NP (800 μM for 1 h 30 min).

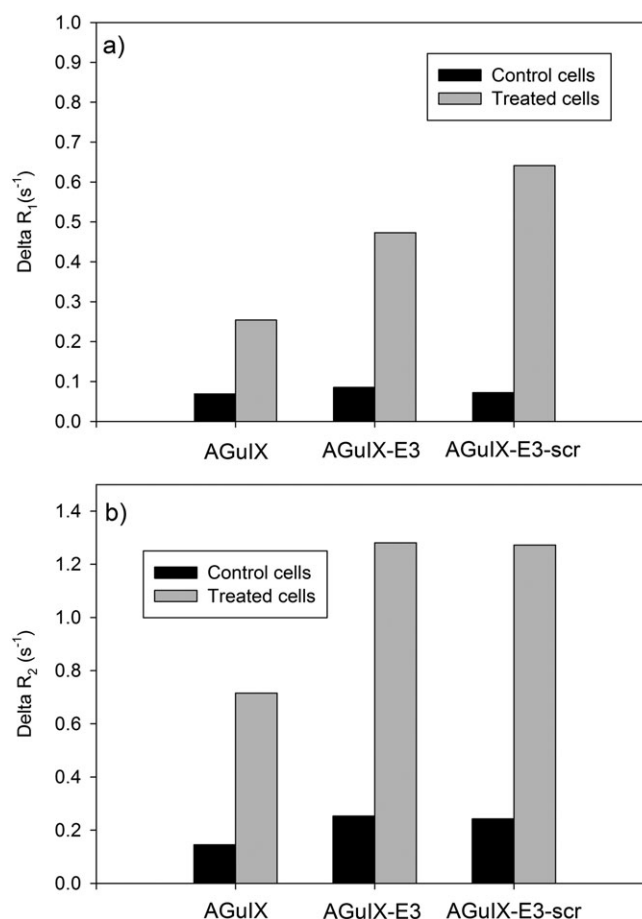


Figure 9. ΔR_1 (a) and ΔR_2 (b) of 10^7 AGuIX-incubated cells suspended in 80 μ L of gelatin at 15 °C and 60 MHz. $\Delta R_{1,2}$ are defined as the differences between relaxation rates of AGuIX-incubated cells and relaxation rates of non-incubated cells.








	Control cells				Treated-cells		
	No NP	AGuIX	AGuIX-E3	AGuIX-E3Sc	AGuIX	AGuIX-E3	AGuIX-E3Sc
							
R_1 (s ⁻¹)	0.326	0.353	0.375	0.352	0.408	0.475	0.563

Figure 10. 7 T MRI T_1 -weighted images and relaxation rates of 10^7 incubated cell pellets suspended in 80 μ L of gelatin (RARE imaging protocol, $TR = 440$ ms, $TE = 9.1$ ms).

3.8. In vitro characterization of targeting efficiency

In order to confirm the specificity of grafted AGuIX nanoparticles, they were tested in presence of apoptotic cells. The apoptosis targeting efficiency of grafted AGuIX nanoparticles was first evaluated using fluorescence microscopy on Jurkat cells treated with 2 μ M of camptothecin over 24 h. PI was used to stain the DNA of necrotic and late apoptotic state cells. Figure 8(a) illustrates that, after treatment, a large proportion of cells were in an early apoptotic state, but also in late apoptotic and necrotic states. In fact, both conditions overexpose phosphatidylserine on the cell surface. Double-stained cells were also observed (late apoptosis) (see supporting information).

In the presence of RITC-labelled nanoparticles (Fig. 8(b)), treated cells were effectively stained by vectorized nanoparticles. However the specificity of AGuIX-(L)-E3 cannot be confirmed, due to the higher targeting efficiency by E3 scramble-AGuIX nanoparticles. Targeting of treated cells by vectorized AGuIX was also confirmed by relaxometry (60 MHz, 15 °C) (Fig. 9) and MRI study of incubated pellets, for which R_1 is 1.9 times higher when AGuIX-E3 is incubated and 2.2 times higher when AGuIX-E3Sc is present as compared with AGuIX-treated cells. For control cells, a slight increase (15% of maximum) of R_1 can be related to the presence of necrotic or late apoptotic cells in the culture. Similarly, a larger increase of R_2 is observed when

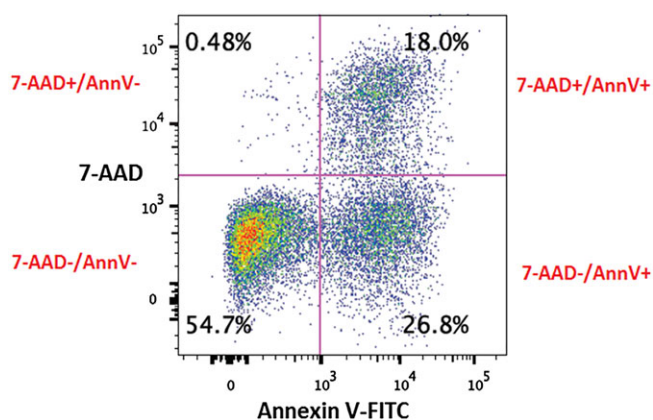


Figure 11. FACS diagram describing fluorescence intensity signal of each detected cell under annexin V-FITC and 7-AAD emission values in one sample.

AGuIX nanoparticles are grafted with the peptides. Longitudinal relaxation rates and the contrast in T_1 -weighted images at 7T confirmed that treated cells seem to be better targeted by AGuIX grafted with E3 scramble (Fig. 10).

3.9. Flow cytometry (FACS)

3.9.1. Cells in early state of apoptosis

The FACS experiment allows discrimination of cells through their staining and their morphological conditions. Indeed the proportion in each cell state is easily recognized, making possible the analysis of targeting level for each single state of cells by labelled AGuIX nanoparticles. A first experiment was performed to determine the best treatment to generate a high proportion of Jurkat cells in the early state of apoptosis, described as '7-AAD⁻/AnnV⁺', unstained by 7-AAD and stained by annexin V-FITC. The Jurkat cell treatment with 5 μ M of camptothecin for 2 h was chosen. The average proportion in each cell staining is described in Table 5. A FACS diagram (Fig. 11) illustrated each cell population according to its staining.

A cell treatment with the same conditions as were used in microscopy and relaxometry experiments (2 μ M for 24 h) generates a higher proportion of Jurkat cells in the 7-AAD⁺/AnnV⁺ state (necrotic and late apoptotic cells) (see supporting information).

3.9.2. Analysis of the specific apoptotic cells targeted by labelled AGuIX

The FACS experiment was used to evaluate the specificity of labelled and vectorized AGuIX for apoptotic cells. Cells were first treated with camptothecin at 5 μ M for 2 h and incubated with nanoparticles. For this experiment, the population in 7-AAD⁻/AnnV⁺ stained cells was $14.05 \pm 1.28\%$ and that of 7-AAD⁺/AnnV⁺

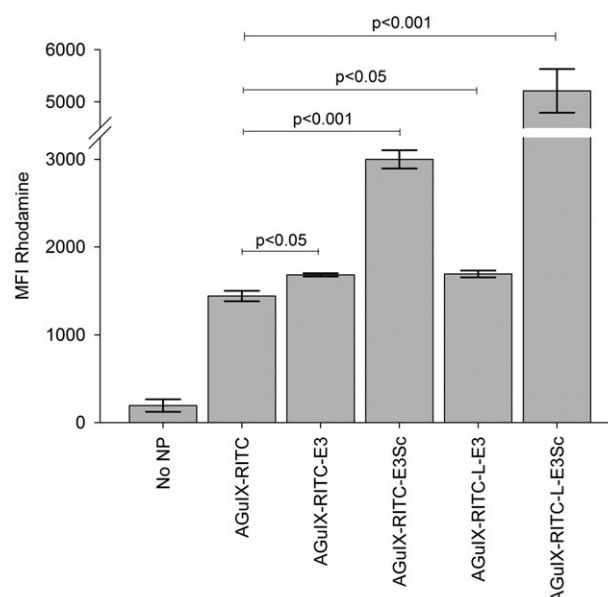


Figure 12. Fluorescence intensity median of rhodamine for early apoptotic cells in each incubated cell sample with RITC-labelled AGuIX.

was $33.17 \pm 2.15\%$. The fluorescence intensity median in rhodamine for each cell population was measured (Fig. 12).

These experiments have been carried out considering an average of fluorescence medians measured for each sample. They show that on early apoptotic cells the measured fluorescence for grafted AGuIX is significantly ($p < 0.05$) higher than the fluorescence observed for non-grafted AGuIX nanoparticles. They show also that the fluorescence of AGuIX grafted with E3 scramble peptide is larger than that of AGuIX grafted with E3 peptide when the targeting of early apoptotic cells is considered. They also show the better targeting efficiency when a spacer is introduced between the nanoparticle and the E3 scramble peptide.

However, these analyses have been made on a cell sample where the apoptotic cells are concomitantly targeted by annexin V-FITC and the peptide-functionalized nanoparticles, leading to a possible competitive phenomenon.

4. CONCLUSION

Grafting of peptides has been confirmed by chemical and biological characterizations. Indeed, a general enhancement of relaxivity was observed after the AGuIX functionalization, the nanoparticle size increased and the targeting of Jurkat apoptotic cells was confirmed by fluorescence microscopy, relaxivity and flow cytometry analysis. However, the *in vitro* tests performed on our cells seemed to highlight a better targeting efficiency of AGuIX grafted with E3 scramble than E3. This could be explained by a possible modification of the spatial configuration of

Table 5. The average percentage of each kind of stained cells measured by flow cytometry in three cell samples

Treatment	% 7-AAD ⁺ /AnnV ⁻ Fragmented cells	% 7-AAD ⁺ /AnnV ⁺ Necrotic and late apoptotic cells	% 7-AAD ⁻ /AnnV ⁺ Early apoptotic cells	% 7-AAD ⁻ /AnnV ⁻ Unstained cells
Camptothecin 2 h 5 μ M	1.1 ± 0.9	18.1 ± 0.2	25.7 ± 1.5	54.9 ± 0.4

peptides after their grafting on AGuIX nanoparticles, which could have modified their affinity for the target. In perspective, 3D modelling of spatial configurations of AGuIX-E3 and AGuIX-E3Sc considering their interaction with phosphatidylserine should be performed.

Acknowledgements

This work was performed with the financial support of the Fonds National pour la Recherche Scientifique (F.R.S.-FNRS), FEDER, the Walloon Region, the COST Action TD1004 'Theranostics imaging and therapy: an action to develop novel nanosized systems for imaging-guided drug delivery', the Centre for Microscopy and Molecular Imaging (CMMI), supported by the European Regional Development Fund of the Walloon Region, and the ARC and UIAP programs. We also wish to thank Marie Plissonneau, Corinne Piérart, Fabien Rossetti, Fabian Rouffiange and Mathieu Roch for their contributions. We would also like to express our gratitude to French program ANR-12-RP10-0010 Multimode for funding.

REFERENCES

- Mignot A, Truillet C, Lux F, Sancey L, Louis C, Denat F, Boschetti F, Bocher L, Gloter A, Stéphan O, Antoine R, Dugourd P, Luneau D, Novitchi G, Figueiredo LC, De Moraes PC, Bonneviot L, Albela B, Ribot F, Van Lokeren L, Déchamps-Olivier I, Chuburu F, Lemerrier C, Villiers C, Marche PN, Le Duc G, Roux S, Tillement O, Perriat P. A top-down synthesis route to ultrasmall multifunctional Gd-based silica nanoparticles for theranostic applications. *Chemistry* 2013; 19: 6122–6136.
- Sancey L, Lux F, Kotb S, Roux S, Dufort S, Bianchi A, Crémillieux Y, Fries P, Coll J-L, Rodriguez-Lafrasse C, Janier M, Dutreix M, Barberi-Heyob M, Boschetti F, Denat F, Louis C, Porcel E, Lacombe S, Le Duc G, Deutsch E, Perfettini J-L, Detappe A, Verry C, Berbeco R, Butterworth KT, McMahon SJ, Prise KM, Perriat P, Tillement O. The use of theranostic gadolinium-based nanoprobe to improve radiotherapy efficacy. *Br J Radiol* 2014; 87(1041): 20140134.
- Bechet D, Auger F, Couleaud P, Marty E, Ravasi L, Durieux N, Bonnet C, Plénat F, Frochot C, Mordon S, Tillement O, Vanderesse R, Lux F, Perriat P, Guillemain F, Barberi-Heyob M. Multifunctional ultrasmall nanoplateforms for vascular-targeted interstitial photodynamic therapy of brain tumors guided by real-time MRI. *Nanomedicine Nanotechnol Biol Med* 2015; 11(3): 657–670.
- Lux F, Mignot A, Mowat P, Louis C, Dufort S, Bernhard C, Denat F, Boschetti F, Brunet C, Antoine R, Dugourd P, Laurent S, Vander Elst L, Muller RN, Sancey L, Josseland V, Coll J-L, Stupar V, Barbier E, Rémy C, Broisat A, Ghezzi C, Le Duc G, Roux S, Perriat P, Tillement O. Ultrasmall rigid particles as multimodal probes for medical applications. *Angew Chem Int Ed Engl* 2011; 50(51): 12299–12303.
- Sancey L, Kotb S, Truillet C, Appaix F, Marais A, Thomas E, Van der Sanden B, Klein J, Laurent B, Cottier M, Antoine R, Dugourd P, Panczer G, Lux F, Perriat P, Motto-Ros V, Tillement O. Long-term in vivo clearance of gadolinium-based AGuIX nanoparticles and their biocompatibility after systemic injection. *ACS Nano* 2015; 9(3): 2477–2488. doi:10.1021/acsnano.5b00552.
- Bridot J-L, Dayde D, Riviere C, Mandon C, Billotey C, Lerondel S, Sabattier R, Cartron G. Hybrid gadolinium oxide nanoparticles combining imaging and therapy. *J Mater Chem* 2009; 19(16): 2328–2335. doi:10.1039/B815836C.
- Benachour H, Bastogne T, Toussaint M, Chemli Y, Sève A, Frochot C, Lux F, Tillement O, Vanderesse R, Barberi-Heyob M. Real-time monitoring of photocytotoxicity in nanoparticles-based photodynamic therapy: a model-based approach. *PLoS One* 2012; 7(11): e48617. doi:10.1371/journal.pone.0048617.
- Kobayashi K, Usami N, Porcel E, Lacombe S, Le Sech C. Enhancement of radiation effect by heavy elements. *Mutat Res* 2010; 704(1–3): 123–131.
- Rima W, Sancey L, Aloy MT, Armandy E, Alcantara GB, Epicier T, Malchère A, Joly-Pottuz L, Mowat P, Lux F, Tillement O, Burdin B, Rivoire A, Boulé C, Anselme-Bertrand I, Pourchez J, Cottier M, Roux S, Rodriguez-Lafrasse C, Perriat P. Internalization pathways into cancer cells of gadolinium-based radiosensitizing nanoparticles. *Biomaterials* 2013; 34(1): 181–195. doi:10.1016/j.biomaterials.2012.09.029.
- Luchette M, Korideck H, Makrigiorgos M, Tillement O, Berbeco R. Radiation dose enhancement of gadolinium-based AGuIX nanoparticles on HeLa cells. *Nanomedicine* 2014; 10(8): 1751–1755.
- Porcel E, Tillement O, Lux F, Mowat P, Usami N, Kobayashi K, Furusawa Y, Le Sech C, Li S, Lacombe S. Gadolinium-based nanoparticles to improve the hadrontherapy performances. *Nanomedicine* 2014; 10(8): 1601–1608.
- Le Duc G, Miladi I, Alric C, Mowat P, Bräuer-Krisch E, Bouchet A, Khalil E, Billotey C, Janier M, Lux F, Epicier T, Perriat P, Roux S, Tillement O. Toward an image guided microbeam radiation therapy using gadolinium-based nanoparticles. *ACS Nano* 2011; 5(12): 9566–9574.
- Carrillo-Carrión C, Nazarens M, Paradinas SS, Carregal-Romero S, Almendral MJ, Fuentes M, Pelaz B, Del Pino P, Hussain I, Clift MJ, Rothen-Rutishauser B, Liang X-J, Parak WJ. Metal ions in the context of nanoparticles toward biological applications. *Curr Opin Chem Eng* 2014; 4: 88–96.
- Maeda H, Wu J, Sawa T, Matsumura Y, Hori K. Tumor vascular permeability and the EPR effect in macromolecular therapeutics: a review. *J Control Release* 2000; 65(1/2): 271–284.
- Benachour H, Sève A, Bastogne T, Frochot C, Vanderesse R, Jasiewicz J, Miladi I, Billotey C, Tillement O, Lux F, Barberi-Heyob M. Multifunctional peptide conjugated hybrid silica nanoparticles for photodynamic therapy and MRI. *Theranostics* 2012; 2(9): 889–904.
- Morlieras J, Dufort S, Sancey L, Truillet C, Mignot A, Rossetti F, Dentamaro M, Laurent S, Vander Elst L, Muller RN, Antoine R, Dugourd P, Roux S, Perriat P, Lux F, Coll J-L, Tillement O. Functionalization of small rigid platforms with cyclic RGD peptides for targeting tumors overexpressing $\alpha\beta_3$ -integrins. *Bioconjug Chem* 2013; 24(9): 1584–1597.
- Morlieras J, Chezal J-M, Miot-Noirault E, Roux A, Heinrich-Balard L, Cohen R, Tarrit S, Truillet C, Mignot A, Hachani R, Kryza D, Antoine R, Dugourd P, Perriat P, Janier M, Sancey L, Lux F, Tillement O. Development of gadolinium based nanoparticles having an affinity towards melanin. *Nanoscale* 2013; 5(4): 1603–1615.
- Elmore S. Apoptosis: a review of programmed cell death. *Toxicol Pathol* 2007; 35(4): 495–516.
- Majno G, Joris I. Apoptosis, oncosis, and necrosis. An overview of cell death. *Am J Pathol* 1995; 146(1): 3–15.
- Burtea C, Laurent S, Lancelot E, Ballet S, Murariu O, Rousseaux O, Port M, Vander Elst L, Corot C, Muller RN. Peptidic targeting of phosphatidylserine for the MRI detection of apoptosis in atherosclerotic plaques. *Mol Pharm* 2009; 6(6): 1903–1919.
- Khan KH, Blanco-Codesido M, Molife LR. Cancer therapeutics: targeting the apoptotic pathway. *Crit Rev Oncol Hematol* 2014; 90(3): 200–19. doi:10.1016/j.critrevonc.2013.12.012.
- Mohammad RM, Muqbil I, Lowe L, Yedjou C, Hsu H-Y, Lin L-T, Siegelin MD, Fimmognari C, Kumar NB, Dou QP, Yang H, Samadi AK, Russo GL, Spagnuolo C, Ray SK, Chakrabarti M, Morre JD, Coley HM, Honoki K, Fujii H, Georgakilas AG, Amedei A, Nicolai E, Amin A, Ashraf SS, Helferich WG, Yang X, Boosani CS, Guha G, Bhakta D, Ciriolo MR, Aquilano K, Chen S, Mohammed SI, Keith WN, Bilsland A, Halicka D, Nowsheen S, Azmi AS. Broad targeting of resistance to apoptosis in cancer. *Semin Cancer Biol* 2015; 35: 1–26.
- Fulda S. Inhibitor of Apoptosis (IAP) proteins as therapeutic targets for radiosensitization of human cancers. *Cancer Treat Rev* 2012; 38(6): 760–766.
- Soon S, Kim Y, Jin E, Hwa S, Choi J, Park J, Hee J, Jin K, Park J, Ji H, Jung E, Jin J, Jin D, Suh N, Cho D, Shin J, Yeol S, Kim BM, Jeong S, Kyung E. Ibulocydine sensitizes human cancers to radiotherapy by induction of mitochondria-mediated apoptosis. *Radiother Oncol* 2014; 112(2): 295–301. doi:10.1016/j.radonc.2014.07.005.
- Bordón E, Henríquez-Hernández LA, Lara PC, Ruiz A, Pinar B, Rodríguez-Gallego C, Lloret M. Prediction of clinical toxicity in locally advanced head and neck cancer patients by radio-induced apoptosis in peripheral blood lymphocytes (PBLs). *Radiat Oncol* 2010; 5: 4.
- Laumonier C. Imagerie moléculaire: recherche de vecteurs spécifiques de l'apoptose par la méthode du phage display. PhD Thesis. University of Mons-Hainaut, 2005; p. 111.
- Laumonier C, Segers J, Laurent S, Michel A, Coppée F, Belayew A, Vander Elst L, Muller RN. A new peptidic vector for molecular

- imaging of apoptosis, identified by phage display technology. *J Biomol Screen* 2006; 11(5): 537–545.
28. Van Koninckxloo A, Henoumont C, Laurent S, Muller RN, Vander EL. NMR chemical shift study of the interaction of selected peptides with liposomal and micellar models of apoptotic cells. *J Biol Inorg Chem* 2014; 19(8): 1367–1376.
 29. Le Duc G, Roux S, Paruta-Tuarez A, Dufort S, Brauer E, Marais A, Truillet C, Sancey L, Perriat P, Lux F, Tillement O. Advantages of gadolinium based ultrasmall nanoparticles vs molecular gadolinium chelates for radiotherapy guided by MRI for glioma treatment. *Cancer Nanotechnol* 2014; 5: 4.
 30. Moussaron A, Vibhute S, Bianchi A, Gündüz S, Kotb S, Sancey L, Motto-Ros V, Rizzitelli S, Crémillieux Y, Lux F, Logothetis NK, Tillement O, Angelovski G. Ultrasmall nanoplateforms as calcium-responsive contrast agents for magnetic resonance imaging. *Small* 2015; 11(37): 4900–4909. doi:10.1002/sml.201500312.
 31. Wiener EC, Brechbiel MW, Brothers H, Magin RL, Gansow OA, Tomalia DA, Lauterbur PC. Dendrimer-based metal chelates: a new class of magnetic resonance imaging contrast agents. *Magn Reson Med* 1994; 31(1): 1–8.
 32. Burton DR, Forsen S, Karlstrom G, Dwek RA. Proton relaxation enhancement (PRE) in biochemistry – critical survey. *Prog Nucl Magn Reson Spectrosc* 1979; 13: 1–45.
 33. Kruk D, Kowalewski J. General treatment of paramagnetic relaxation enhancement associated with translational diffusion. *J Chem Phys* 2009; 130(17): 1–13.
 34. Helm L. Relaxivity in paramagnetic systems: theory and mechanisms. *Prog Nucl Magn Reson Spectrosc* 2006; 49(1): 45–64.
 35. Tei L, Gugliotta G, Baranyai Z, Botta M. A new bifunctional Gd^{III} complex of enhanced efficacy for MR-molecular imaging applications. *Dalton Trans R Soc Chem* 2009; 44: 9712–9714.
 36. Mieville P, Jaccard H, Reviriego F, Tripier R, Helm L. Synthesis, complexation and NMR relaxation properties of Gd³⁺ complexes of Mes (DO3A)₃. *Dalton Trans R Soc Chem* 2011; 40(16): 4260–4267.
 37. Filippi M, Remotti D, Botta M, Terreno E, Tei L. GdDOTAGA(C₁₈)₂: an efficient amphiphilic Gd(III) chelate for the preparation of self-assembled high relaxivity MRI nanoprobables. *Chem Commun R Soc Chem* 2015; 51(98): 17455–17458.
 38. Kieler F, Tei L, Terreno E, Botta M. Large relaxivity enhancement of paramagnetic lipid nanoparticles by restricting the local motions of the Gd^{III} chelates. *J Am Chem Soc* 2010; 132(23): 7836–7837.
 39. Vander Elst L, Sessoye A, Laurent S, Muller RN. Can the theoretical fitting of the proton-nuclear-magnetic-relaxation-dispersion (proton NMRD) curves of paramagnetic complexes be improved by independent measurement of their self-diffusion coefficients? *Helv Chim Acta* 2005; 88: 574–587.
 40. Laurent S, Henoumont C, Vander Elst L, Muller RN. Synthesis and physicochemical characterisation of Gd-DTPA derivatives as contrast agents for MRI. *Eur J Inorg Chem* 2012; 12: 1889–1915.
 41. Schmidt H, Scholze H, Kaiser A. Principles of hydrolysis and condensation reaction of alkoxysilanes. *J Non-Cryst Solids* 1984; 63: 1–11.
 42. Truillet C, Lux F, Tillement O, Dugourd P, Antoine R. Coupling of HPLC with electrospray ionization mass spectrometry for studying the aging of ultrasmall multifunctional gadolinium-based silica nanoparticles. *Anal Chem* 2013; 85(21): 10440–10447.
 43. Frangioni J. *In vivo* near-infrared fluorescence imaging. *Curr Opin Chem Biol* 2003; 7(5): 626–634.
 44. Parmelee DJ, Walovitch RC, Ouellet HS, Lauffer RB. Preclinical evaluation of the pharmacokinetics, biodistribution, and elimination of MS-325, a blood pool agent for magnetic resonance imaging. *Invest Radiol* 1997; 32(12): 741–747.
 45. Henrotte V, Laurent S, Gabelica V, Vander Elst L, Depauw E, Muller RN. Investigation of non-covalent interactions between paramagnetic complexes and human serum albumin by electrospray mass spectrometry. *Rapid Commun Mass Spectrom* 2004; 18(17): 1919–1924.
 46. Laurent S, Vander Elst L, Muller RN. Comparative study of the physicochemical properties of six clinical low molecular weight gadolinium contrast agents. *Contrast Media Mol Imaging* 2006; 1(3): 128–137.

SUPPORTING INFORMATION

Additional supporting information can be found in the online version of this article at the publisher's website.